Catalysis Today 413-415 (2023) 113986

Contents lists available at ScienceDirect

Catalysis Today

journal homepage: www.elsevier.com/locate/cattod

Silica-modified bismutite nanoparticles for enhanced adsorption and faster solar photocatalytic degradation of methylene blue

Jibin Antony [a], Susana Villa Gonzalez [b], Sulalit Bandyopadhyay [a], Jia Yang [a], Magnus Rønning [a,*]

[a] Department of Chemical Engineering, Norwegian University of Science and Technology, NO-7491, Trondheim, Norway
[b] Department of Chemistry, Norwegian University of Science and Technology, NO-7491, Trondheim, Norway

ARTICLE INFO

Keywords:
Photocatalysis
Methylene blue
Bismutite
Silica
Enhanced adsorption
Faster mineralization

ABSTRACT

Herein, we report the synthesis of silica-modified self-assembled structures of bismutite (BSC) through a facile hydrothermal route. The incorporation of silica into the hybrid led to improved adsorption of cationic methylene blue (MB) dye due to electrostatic and hydrogen bond interactions with the silanol groups present on the catalyst surface. The enhanced adsorption of MB on the catalyst ensured better availability of oxidizing free radicals and charge carriers on the catalyst surface for photocatalytic degradation of MB, resulting in faster mineralization of organic species in the presence of solar light. The faster degradation could be observed as a blue shift in the absorbance of degradation intermediates during the reaction and was supported by further analysis using a mass spectrometer. Results from total organic carbon (TOC) analysis indicated 20 % better mineralization in presence of silica-modified BSC hybrids. This study reveals the importance of controlled incorporation of a suitable adsorbent to the semiconductor photocatalyst to overcome the sluggish reaction kinetics under sunlight, thus promoting faster degradation of organic species.

1. Introduction

The rapid increase in industrialization has led to accumulation of various hazardous pollutants in the environment. Among these pollutants, organic dyes are one of the major contaminants of industrial wastewater, which are primarily released from textiles, paint, paper manufacturing and other similar industries [1,2]. Methylene blue (MB) is one such dye that has gained lot of attention due to its broad range of applications such as in temporary hair dyes, pigments, paints and coloring paper [3,4]. These organic contaminants are toxic and being non-biodegradable, persist in the environment for long periods, thereby posing a serious threat to the ecosystem and to human health [5–9]. Owing to their high chemical stability, they form complexes by combining with various heavy metal oxides and hence needs to be treated before discharge [10]. However, the majority of these dyes cannot be entirely mineralized by traditional physico-chemical and biological treatment methods [11]. The research and development in this field has given rise to a new class of processes called “advanced oxidation processes” (AOPs), photocatalysis being one of the significant processes [12].

The development of highly efficient catalytic systems is the key to photocatalytic degradation of industrial wastewater. Bismuth-based nanostructured particles such as Bi_2WO_6, $BiVO_4$, BiOX (X = Cl, Br, I) and $(BiO)_2CO_3$ have previously been studied for photocatalytic degradation of organic dyes such as methyl orange, rhodamine B and MB [13–16]. Among these, Aurivillius-type BSC with alternating $(Bi_2O_2)^{2+}$ and CO_3^{2-} layering has drawn particular research interest owing to its unique anisotropic crystal structure and internal static electric field effect, which favors photoinduced charge transfer and separation [17]. However, application as a photocatalyst has primarily been limited to the UV spectrum due to its relatively wide bandgap of 3.12 eV, which would mean less than 5 % of the solar spectrum will have sufficient energy to activate the photocatalyst. This indicates the importance of specific tailoring of the properties of the photocatalyst for improved light harvesting and enhanced adsorption of contaminants leading to better solar energy conversion efficiency.

It is well known that the surface area and number of active sites offered by the catalyst have significant effect on the catalytic degradation process as this would lead to better availability of charge carriers and free radical species to the organic dye [18]. Silica is known to be a good adsorbent due to porous structure and high surface-to-volume ratio [19,20]. Previous works have reported enhanced adsorption of cationic

* Corresponding author.
E-mail address: magnus.ronning@ntnu.no (M. Rønning).

https://doi.org/10.1016/j.cattod.2022.12.017
Received 16 July 2022; Received in revised form 18 September 2022; Accepted 21 December 2022
Available online 26 December 2022

organic dyes such as MB and methyl violet on mesoporous silica and silica-modified nanocomposites due to electrostatic and hydrogen bond interactions between the cationic dyes and the high amount of exposed silanol groups present on the catalyst surface [21–24]. Anderson and Bard reported mixed oxides of TiO_2/SiO_2 prepared by sol-gel method to improve photocatalytic decomposition of phenol as a result of enhancement of local TiO_2 sites [25]. Furthermore, a recent investigation by Wang et al. reported silica to induce defects such as oxygen vacancies in supported mixed-phase TiO_2 which led to enhanced performance in the photocatalytic degradation of phenol under visible light irradiation [26]. However, most of the studies until now involving the incorporation of silica have either been performed via conventional sol-gel hydrolysis and coprecipitation techniques or via depositing pre-synthesized silica particles which might suffer from the limitation of proximity of adsorption sites on the catalyst to the oxidant species being generated at the catalytically active sites [20,27,28]. Moreover, the effect of silica addition has so far been primarily investigated on titania and have not been extended to other photocatalytic materials. This highlights the significance of developing new synthesis methods for incorporating silica into hybrid structures using methods which would help in obtaining an intimate interface contact leading to more efficient photocatalysts.

Here, we report the synthesis of silica-modified self-assembled hybrid structures of BSC through a facile hydrothermal route. The silica-modified hybrids were synthesized by modifying the synthesis protocol for BSC with the addition of sodium silicate. Two different hybrids with varying silica content were synthesized and systematically characterized by several characterization tools to investigate their size, morphology, crystalline phase, composition, surface charge, surface area and optical properties among others. The photocatalytic activity of these hybrids was then investigated in MB degradation experiments performed under simulated sunlight at AM 1.5 G conditions. We believe that the controlled incorporation of silica into BSC or other semiconductor NPs of interest has the prospective to tackle the sluggish photocatalytic mineralization kinetics of organic dyes under sunlight, and thus lead to better catalyst efficiencies.

2. Experimental section

2.1. Synthesis of BSC / BSC-SiO_2 nanoparticles

BSC nanoparticles were synthesized by following a previously reported method [17]. Briefly 4.8252 g of bismuth (III) nitrate pentahydrate, 2.5 g of urea and 0.387 g of sodium citrate tribasic dihydrate were dispersed in 30 ml of 1 M NaOH by magnetic stirring at 900 rpm for 30 min. Following this step, the suspension was transferred into a 100 ml teflon liner and the autoclave was placed in an oven at 180 ℃ for 6 h, after which it was allowed to cool down naturally to room temperature. The obtained catalyst particles were washed thrice each in DI water and ethanol respectively, followed by drying at 80 ℃ for 12 h.

BSC-silica hybrid NPs were synthesized using the same approach except for replacing a certain volume of 1 M NaOH solution with sodium silicate solution. Two hybrids containing silica were synthesized by adding 100 μl and 250 μl of sodium silicate solution and have been denoted as BSC_NS100 and BSC_NS250, respectively. Some experiments with higher volumes of sodium silicate solution were also performed which gave rise to a chunky mass after the hydrothermal treatment and could not be characterized, hence not reported here.

3. Results and discussion

3.1. Morphology characterization

The size and morphology of the pristine BSC particles and the ones synthesized in presence of sodium silicate were analyzed using a Hitachi SU9000 ST(E)M in SEM mode and are shown in Fig. 1(a-c). The disc-like shape of pristine BSC NPs observed in Fig. 1(a) were in congruence with the structures reported by Xiao et al. [17]. The BSC nanodiscs (NDs) had an average size of 330 ± 130 nm and thickness of 50 ± 8 nm. The addition of 100 μl sodium silicate to the reaction mixture was found to induce self-assembly of these disc-like particles as can be observed for BSC_NS100 in Fig. 1(b). However, the thickness of these discs was found to considerably reduce to 29 ± 2 nm. Further addition of sodium silicate solution (250 μl) led to 3D stacking of the NDs and gave rise to flower-like hierarchical structures as shown in Fig. 1(c). Although these structures were larger in size (1.6 ± 0.2 μm), the NDs constituting the discs were found to be much thinner (16 ± 2 nm). No significant differences could be observed in the lateral dimensions of the NDs with addition of sodium silicate solution. Therefore, self-assembly and thinning of BSC NDs were observed to be the main outcomes of incorporation of silica on the BSC morphology. Fig. S1 shows SEM images of the different BSC NPs at higher magnification providing better visualization of the thinning of NDs induced by the incorporation of silica.

3.2. Composition analysis

The elemental composition of the samples was analyzed using an EDX spectrometer and an increasing content of elemental silicon was confirmed in the samples synthesized under higher volumes of sodium silicate as shown in the map spectrum in Fig. S2 and Table S1. The elemental maps of BSC, BSC_NS100 and BSC_NS250 are shown in Fig. S3, S4 and S5 respectively. An even distribution of silicon in all elemental maps obtained confirmed uniform incorporation of silica in all the hybrids.

3.3. Crystalline structure

The X-ray diffraction (XRD) patterns of pristine BSC and the silica-modified hybrids are shown in Fig. 2(a). The diffraction peaks correspond well to JCPDS Card No. 41–1488 for tetragonal bismutite ($Bi_2O_2CO_3$) with a = b= 3.867 Å; c = 13.686 Å; and space group I_4/mm) [17]. The sharp peaks for BSC indicate phase purity and high crystallinity of the sample. With addition of sodium silicate, no shift in the peaks could be observed, thus indicating phase purity. However, the

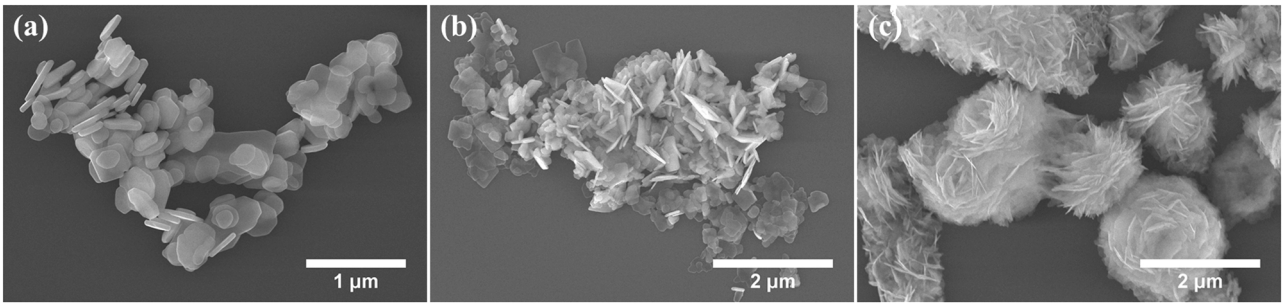

Fig. 1. Representative SEM images of BSC NPs synthesized at different conditions. (a) BSC, (b) BSC_NS100, (c) BSC_NS250.

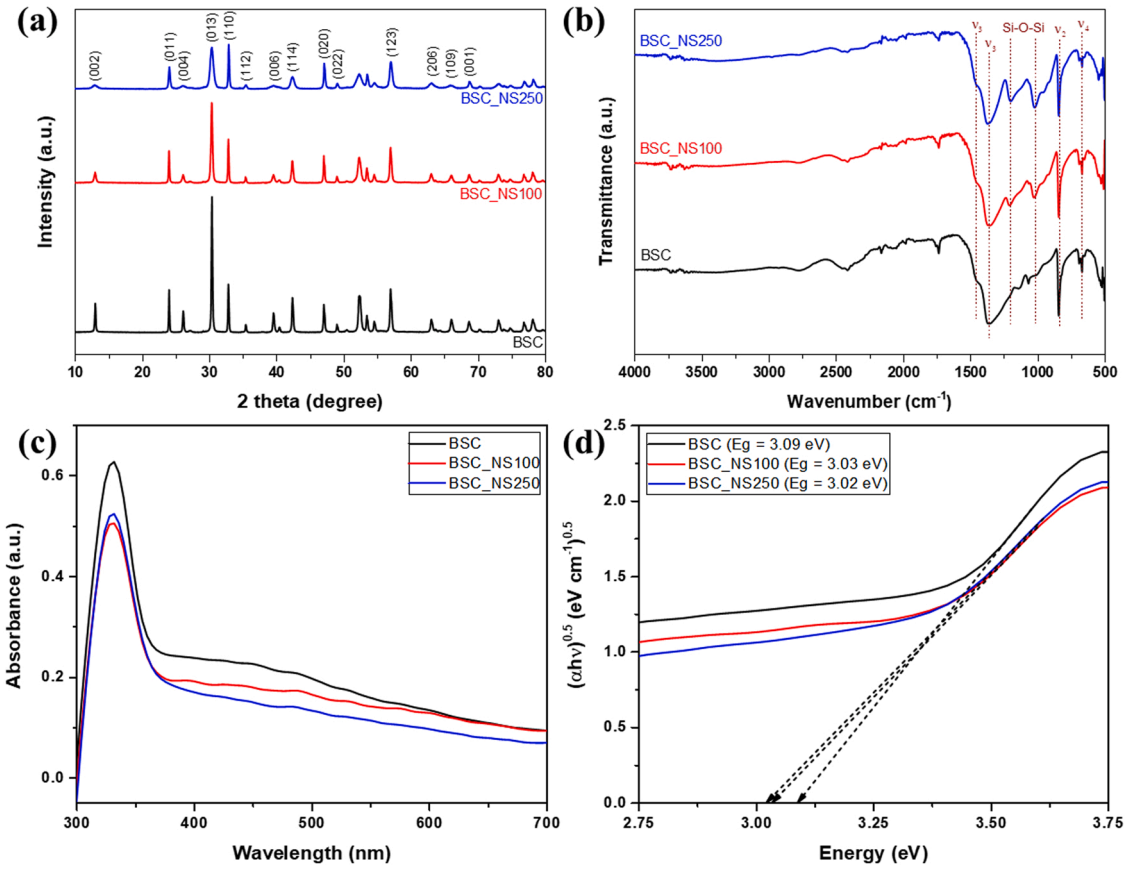

Fig. 2. (a) XRD patterns, (b) FT-IR spectra, (c) UV-Vis absorption spectra and (d) Tauc plot showing the optical bandgap of the different BSC samples. Tauc plot was obtained by plotting $(\alpha h\nu)^{0.5}$ with the photon energy = $h\nu$ (where h is the Planck's constant, α is the absorption coefficient, ν is the frequency, and 0.5 refers to the direct bandgap transitions present in BSC samples. The optical bandgap of the catalysts was obtained by extrapolating the linear region of the plot to the abscissa.

crystallinity of the samples was observed to reduce, which could be attributed to the presence of amorphous silica on BSC. Silica generally gives a broad diffraction peak between $2\theta = 0°$ and 20°. However, this could not be observed presumably due to the relatively low content of silica present.

3.4. FT-IR analysis

The presence of silica and the purity of the samples were further confirmed with the help of Fourier Transform Infrared (FT-IR) Spectroscopy as shown in Fig. 2(b). Two additional peaks at wavenumbers 1010 cm^{-1} and 1195 cm^{-1} were observed for the silica-modified hybrids, which could be assigned to Si-O-Si stretching vibrations. The presence of carbonate ions (CO_3^{2-}) was confirmed by the characteristic peak observed at 1067 cm^{-1} for BSC, which corresponded to the symmetric vibration (ν_1) [29]. However, this peak was not evident in the samples containing silica due to overlapping peaks from Si-O-Si stretching. The peak at 1360 cm^{-1} and the shoulder peak at 1462 cm^{-1} could be assigned to anti-symmetric vibration (ν_3) of CO_3^{2-} ions. The peaks at 838 cm^{-1} and 690 cm^{-1} correspond to out-of-plane bending (ν_2) and in-plane deformation (ν_4) of carbonate ions respectively [14,29]. The broad peak at 2350 cm^{-1} is associated with asymmetric stretching mode of physisorbed CO_2 and the small peaks in the range 3600–3800 cm^{-1} correspond to combination bands [30,31]. No additional vibration peaks were observed, thus confirming the purity of the samples.

3.5. Textural analysis

The textural properties of the samples such as specific surface area, pore volume and average pore diameter were analyzed by N_2 adsorption-desorption isotherms and have been summarized in Table S2. Fig. S6 shows the shape of the isotherm obtained for the different samples. The isotherms belong to Type IV according to IUPAC classification, thus indicating the presence of mesopores [32]. At low relative pressures, the amount adsorbed was observed to increase gradually corresponding to multilayer adsorption. This was followed by a steep rise in the amount adsorbed close to the saturation vapor pressure denoting capillary condensation in the mesopores. The isotherms showed H3 type hysteresis loop, indicating the presence of aggregates of plate-like particles possessing slit-like pores [32]. An increase in specific surface area, specific pore volume and pore diameter could be observed with increasing silica content in the samples, possibly due to thinning of the NDs and the self-assembly into 3D structure. The hysteresis area was found to increase with increasing silica content which is in agreement with the increased pore diameter reported in Table S2.

3.6. Zeta potential

The surface charge of the samples was determined by zeta potential measurements at natural pH as shown in Fig. S7. A catalyst suspension (250 mg/L) of the different catalysts in water showed natural pH values of BSC: 6.2, BSC_NS100: 5.9 and BSC_NS250: 5.9. Pristine BSC NDs have an iso-electric point below 3 and hence would give negative zeta potentials for all pH above 3 [14]. The natural pH of BSC suspension being above 6, showed a negative zeta potential of -23.9 ± 0.6 mV. An increasing net negative charge (-35.8 ± 0.4 mV for BSC_NS100 and -38.0 ± 0.7 mV for BSC_NS250) could be observed with the addition of sodium silicate in the samples. In aqueous suspensions, free unsatisfied bonds of the silica particles are neutralized by OH^- and H^+ species

leading to the formation of silanol groups ($Si(OH)_n$). Above the iso-electric point, the silanol groups would dissociate in water through the reaction shown in Eq. 1 [33]. This further verifies the presence of silica groups on the surface of BSC particles with the addition of sodium silicate.

$$\equiv SiOH + OH^- \leftrightarrow SiO^- + H_2O \quad (1)$$

3.7. Photoluminescence measurements

PL intensities of the samples were compared to investigate the recombination rates and charge carrier lifetime. As can be observed from Fig. S8, the PL intensity of the samples containing silica was lower than for pristine BSC particles pointing to restricted recombination of photo-induced electrons and holes. This is an indication of formation of silica-induced oxygen vacancies in BSC leading to the formation of localized defect energy states in the bandgap, which would act as a sink for the excited electrons thus preventing recombination with holes in the valence band [26]. The restricted recombination of charge carriers is known to lead to enhanced photocatalytic performance due to improved photo-induced charge separation [34].

3.8. UV-vis diffuse reflectance spectroscopy

Diffuse reflectance spectroscopy was performed to record the absorbance of the powder samples, and subsequently obtain their optical bandgaps from the Tauc plot. The optical absorption of the samples is presented in Fig. 2(c). BSC is known to have an indirect bandgap and from the Tauc plot, the bandgap of pristine BSC was found to be 3.09 eV, which is in close agreement to what has previously been reported [17]. A slight lowering of the bandgap (3.09 ⟶ 3.03 ⟶ 3.02 eV) could be observed with increasing silica content in the hybrids as shown in Fig. 2 (d). This again supports the observations made in PL measurements as the presence of silica-induced defect energy states in BSC would lead to a lower effective bandgap.

3.9. Photocatalytic MB degradation

Prior to irradiating the reaction mixture with solar simulated light, an aliquot was withdrawn at the end of 30 min of stirring in dark. The catalyst particles were separated by centrifugation and the supernatant was analyzed with a UV-Vis spectrophotometer. This corresponded to the absorbance at initial time point for the different catalysts as shown in Fig. S9. It could be observed that although the initial concentration of MB dye in all the systems were the same (5 mg/L), the samples containing higher amount of silica showed lower absorbance for the supernatant. This was also evident from the color of the bottom product after centrifugation (shown as inset in Fig. S9), where the catalysts turned more bluish with increasing silica content, thus confirming better adsorption of the dye.

As observed from the zeta potential measurements in Fig. S7, the sample containing highest amount of silica showed more negative potential. This could explain the stronger adsorption of MB molecules as it is a cationic dye. Moreover, from SEM and BET analysis, it was also validated that higher amounts of silica lead to thinner discs with porous flower-like morphology having high surface area and pore volume, thus improving the adsorption capacity of the dye.

After the initial 30 min of attaining adsorption-desorption equilibrium, photocatalytic degradation of MB dye in presence of BSC catalysts was initiated under simulated sunlight. The concentration of remaining dye in solution was obtained using a calibration curve for MB shown in Fig. S10. As shown in Fig. 3(a), in presence of pristine BSC, the absorbance peaks of MB dye were found to follow the parent peak with primary absorbance at 664 nm even after 3 hrs of light irradiation. This is in accordance with previous observations reported in literature which would suggest MB to still be the primary species present in the mixture [14,35]. However, in presence of silica modified BSC, a shift in the peak of MB could be observed immediately after irradiating the sample (as can be seen in Fig. 3(b) and (c)), thereby suggesting faster mineralization of MB. Fig. S11(a) shows the photocatalytic degradation comparison between the different BSC samples. Although BSC_NS250 showed fastest degradation of MB (92.6 % degradation within 1 h), the blue shift in absorbance observed for silica-modified samples indicate the presence of other organic degradation intermediates of MB in the mixture. Since BSC_NS250 showed the best degradation performance, this catalyst was used for further investigations. To verify the photocatalytic nature of these reactions, control experiments were performed with BSC_NS250 in the absence of light and without the catalyst in presence of light as shown in Fig. S11(b). No shift in the absorbance peak and insignificant degradation of MB dye in the control experiments as observed in Fig. S12 proved the photocatalytic nature of the reaction with silica-modified hybrids. Another set of control experiments were performed at a lower concentration of MB dye (3 mg/L), to account for the initial adsorption of the dye due to the presence of silica. The experiments with lower MB dye concentration were performed with BSC as the catalyst to verify that the blue shift in the absorbance peak was silica-induced. No shift in absorbance observed in presence of BSC as catalyst at lower concentrations of MB (Fig. S13) ensured the faster mineralization not just to be an effect of silica-induced adsorption but a result of enhanced photocatalytic properties of the hybrid. The addition of silica has been observed to improve the surface area and pore volume of the particles which would expose the catalytic active sites of BSC. The intimate incorporation of silica into BSC brought about by hydrothermal treatment could lead to better proximity of the adsorbed MB molecules to the oxidant species [18]. In addition, the lower bandgap observed for silica-modified samples suggest the presence of oxygen vacancies in BSC, leading to lower recombination effect of charge carriers and better light absorption properties, which promote faster mineralization of MB. Fig. S14 shows the supernatant after 3 h of reaction with the different

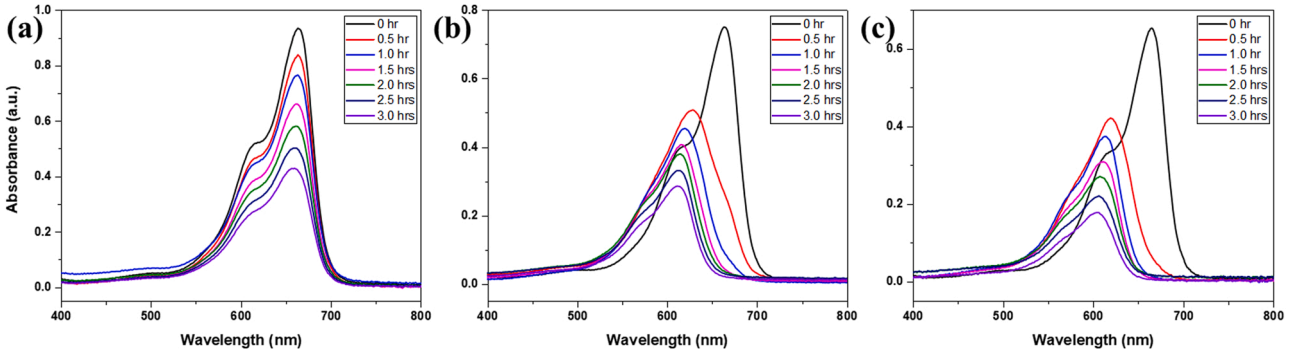

Fig. 3. UV-Vis spectra of MB dye degradation using (a) BSC, (b) BSC_NS100 and (c) BSC_NS250 as photocatalyst under simulated sunlight.

BSC catalysts.

3.10. Mass spectrometry analysis

To further support the observations made from the UV-vis spectra, mass spectrometry analysis of the final decomposed solutions of MB after 3 hrs of reaction was performed for the different BSC catalysts. The mass spectra of pure MB dye solution in Fig. S15(a) depicts the molecular ion at $m/z = 284$ which corresponds to the mass to charge ratio of the MB cation (HR-ESI-MS m/z 284.1221 [M +], calculated for $C_{16}H_{18}N_3S$, 284.1221) The molecular structure of the MB cation is shown in Fig. 4(a). The photocatalytic degradation pathway of MB dye has been previously reported in literature to proceed via demethylation due to the lower bond energy (3.07 eV) associated with the bond between H_3C-N atoms [36]. The successive demethylation reactions would lead to the formation of aromatic degradation intermediates such as Azure A, Azure B, Azure C and thionine as shown in Fig. 4(b-e) [37–39]. All these degradation intermediates have been reported to be associated with a blue shift in the UV-Vis absorbance compared to MB [40–42].

Table S3 shows the exact mass of the intermediates found in samples where pristine BSC particles were used. The tentatively identified intermediate products with mass to charge ratios of 284, 270 and 256 supported the presence of MB, Azure B and Azure A in the mixture. The presence of the peak at 284 was also consistent with the absorbance peaks of MB from UV-Vis spectra where no significant shift could be observed during the reaction. However, in presence of BSC_NS100 and BSC_NS250, the above peaks were not observed as shown in Fig. S15(c, d). Instead, signals of the possible intermediate products (242 and 228) could be observed and tentatively identified, which indicated the presence of degradation products such as Azure C and thionine. This was also consistent with the blue shift observed in the absorbance peaks of MB during photocatalytic reactions in presence of silica-modified hybrids, thus supporting the faster mineralization of MB.

3.11. TOC analysis

The total organic carbon content of the supernatant for the reactions catalyzed by different BSC catalysts were analyzed and the results are shown in Fig. 5. The reduction in TOC content was found to increase with increasing silica content in the hybrid which was in accordance with previous observations. BSC_NS250 showed 48.5 ± 3.6 % reduction in TOC compared to 28.1 ± 3.9 % reduction for pristine BSC particles, thus indicating 20 % better mineralization of organics in presence of silica-modified BSC hybrids.

3.12. Catalyst stability

The stability of a photocatalyst is a key factor for determining its reusability and large-scale applicability. To determine the stability of the BSC_NS250 hybrid, the catalyst was recovered after each run and then reused in three successive runs to degrade fresh MB solution. After each run, the catalyst particles were centrifuged and cleaned once in ethanol before drying overnight in an oven at 80 °C. The particles were then reused without any further modification. Fig. S16 provides a comparison of BSC_NS250 before each successive run. A notable difference in the color of the spent catalyst could be observed as a result of MB adsorption on the catalyst surface. Due to difficulty of recovering the entire batch associated with loss of catalyst during cleaning, the total reaction volume of the successive stability runs was adjusted without changing the catalyst concentration. Fig. S17(a) shows the degradation percentage of MB with BSC_NS250 for 3 successive runs. As can be observed, the BSC_NS250 hybrid catalyst upon reuse retained high catalytic activity (93.2 % and 92.4 % degradation in the 2nd and 3rd runs respectively) which was within the small error margin obtained for the 1st run. A blue-shift in the absorbance peak of MB observed in all successive runs denoted the stability of silica-modified BSC hybrid catalyst in achieving faster mineralization. However, when the TOC of the supernatant after 3 hrs was analyzed, an increase in organic content with subsequent runs could be observed as shown in Fig. S17(b). This could possibly be a result of the adsorbed organic species on the catalyst leaching out during the reaction.

In order to verify this, the spent catalysts were characterized using FT-IR as shown in Fig. S18(a). The FT-IR spectra of the spent catalysts were observed to show additional peaks around 2916 cm^{-1}

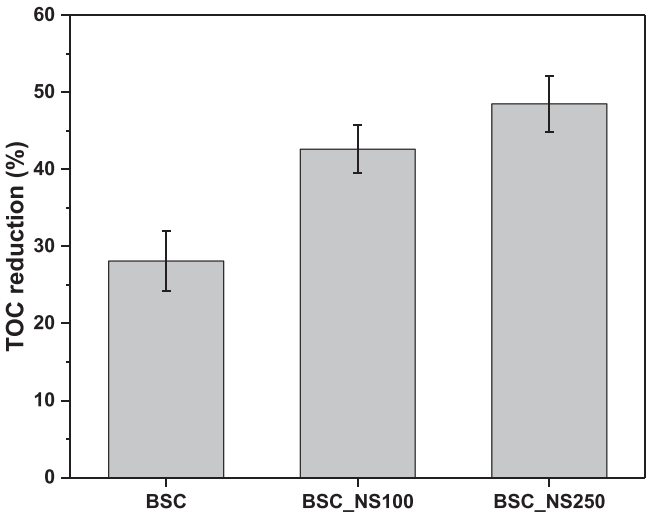

Fig. 5. TOC reduction comparison between the BSC samples. The error bars shown were obtained from three different readings of the same sample.

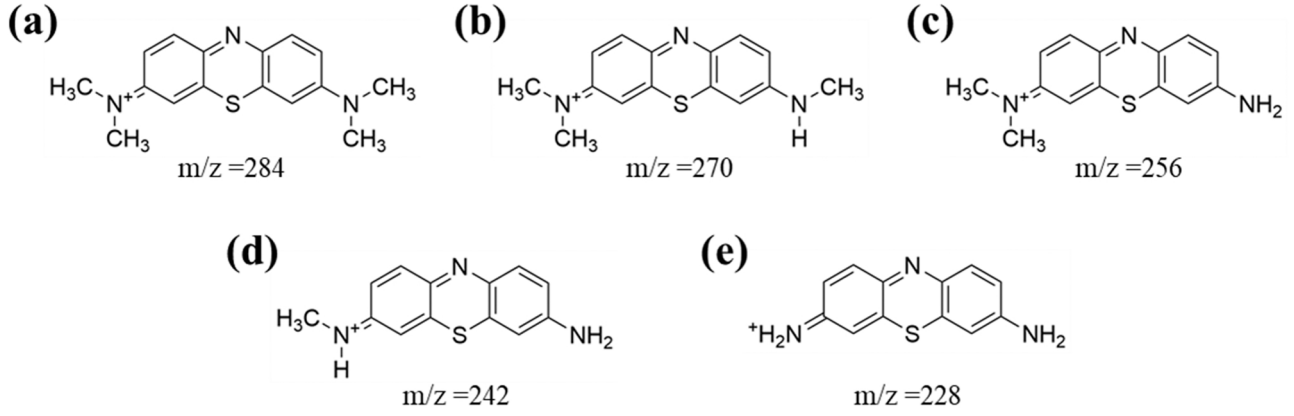

Fig. 4. Structures of cations of intermediate degradation products of MB: (a) MB, (b) Azure B, (c) Azure A, (d) Azure C and (e) Thionine.

corresponding to the C-H stretching vibration and at 1600 cm^{-1} belonging to the skeleton stretching vibration in the benzene ring [43]. The FT-IR spectra of pure methylene blue hydrate is shown in Fig. S18 (b) for reference. The presence of additional peaks corresponding to organic species in the spent catalyst verified the possibility of organic species leaching out during the subsequent runs, thereby leading to an increase in the total organic carbon.

Removing the adsorbed organic species from the catalyst is expected to further improve the catalyst performance by lowering the TOC content in addition to the already visible MB degradation. Techniques such as thermal regeneration and ultrasonic regeneration have been reported in literature to be efficient in recovering spent catalysts [44–46]. However, the thermal stability of BSC also needs to be considered while choosing a thermal recovery method to avoid that the photocatalytic property gets affected.

3.13. Scavenger tests

In order to identify the active species involved in the photocatalytic degradation of MB, scavenging tests were performed using p-benzoquinone (1 mM), 2-propanol (10 mM) and potassium iodide (10 mM) as trapping species for superoxide anion radicals ($\cdot O_2^-$), hydroxyl radicals ($\cdot OH$) and holes (h^+), respectively. As can be observed from Fig. S19, addition of p-benzoquinone and potassium iodide reduced the photocatalytic activity to the maximum extent, which was observed in terms of a delay in the shift of the primary peak of MB at 664 nm, thus indicating $\cdot O_2^-$ and h^+ to be the major active species involved in the degradation. No significant effect observed in presence of 2-propanol suggested $\cdot OH$ to have a minor role in the degradation of MB.

Based on these results, a mechanism for the photocatalytic degradation of MB by silica-modified BSC hybrids can be explained as follows. When the hybrid photocatalyst particles are irradiated with photons having sufficient energy, electrons in the valence band of BSC get transferred to the conduction band. Electrons might also get trapped in the defect energy states within the bandgap, thereby reducing the rate of recombination. These electrons react with dissolved oxygen to form $\cdot O_2^-$ radicals, which along with h^+ in the valence band act as strong oxidizers for the effective degradation of MB adsorbed on silica. Due to the photosensitizer properties of MB, it should be be noted that a photosensitization mechanism could also occur in conjunction with photocatalysis, based on the band structures of BSC and the molecular orbital positions of MB [47].

4. Conclusions

Silica-modified BSC hybrid particles were synthesized by addition of different volumes of sodium silicate solution prior to the hydrothermal process. Incorporating silica into BSC NDs was found to induce thinning of the NDs and self-assembly, leading to the formation of 3D stacked structures with increased surface area, pore volume and pore diameter. Fluorescence measurements showed lower PL intensities for silica-modified hybrids denoting the presence of defect energy states, which was supported by the observed lowering of the bandgap. In addition, the large amounts of silanol groups present on the catalyst surfaces with higher silica content led to better adsorption of cationic MB dye due to the presence of electrostatic and hydrogen bond interactions. Enhanced adsorption of MB on silica-modified BSC hybrid particles could ensure better availability of oxidizing free radicals and charge carriers on the catalyst surface for photocatalytic degradation of MB, resulting in faster mineralization of the organic species in presence of simulated sunlight. Faster mineralization was observed as a blue shift in the absorbance curve of MB which was further supported by mass spectrometry analysis. Furthermore, results from TOC analyzer indicated 20 % better degradation of organic species in presence of silica-modified BSC hybrids. Hence, this work highlights the importance of incorporating a suitable adsorbent to the semiconductor photocatalyst for faster mineralization of organic pollutants and is anticipated to lay foundation for future research in obtaining optimized photocatalysts capable of capturing a wide spectrum of dyes for wastewater remediation.

CRediT authorship contribution statement

Jibin Antony: Conceptualization, Methodology, Validation, Formal analysis, Investigation, Writing – Original Draft, Writing – Review & Editing, Visualization. **Susanna Villa Gonzalez:** Validation, Formal analysis, Investigation, Writing – Review & Editing, Visualization. **Sulalit Bandyopadhyay:** Validation, Writing – Review & Editing, Visualization, Supervision. **Jia Yang:** Validation, Writing – Review & Editing, Visualization, Supervision. **Magnus Rønning:** Conceptualization, Validation, Writing – Review & Editing, Visualization, Supervision, Project Administration, Funding acquisition.

Declaration of Competing Interest

The authors declare that they have no known competing financial interests or personal relationships that could have appeared to influence the work reported in this paper.

Data Availability

Data will be made available on justified request.

Acknowledgements

This project was funded by the Department of Chemical Engineering, NTNU, Trondheim. The Research Council of Norway is acknowledged for the support to the Norwegian Micro- and Nano-Fabrication Facility, NorFab, project number 295864. The authors would also like to acknowledge the Mass Spectrometry Lab at the NV Faculty, NTNU for providing the instrumentation and support with mass spectrometry analysis.

Appendix A. Supporting information

Supplementary data associated with this article can be found in the online version at doi:10.1016/j.cattod.2022.12.017.

References

[1] U. Mahanta, M. Khandelwal, A.S. Deshpande, Appl. Surf. Sci. 576 (2022), 151745.
[2] S. De Gisi, G. Lofrano, M. Grassi, M. Notarnicola, Sustain. Mater. Technol. 9 (2016) 10–40.
[3] M.T. Yagub, T.K. Sen, S. Afroze, H.M. Ang, Adv. Colloid Interface Sci. 209 (2014) 172–184.
[4] X. Zhou, X. Xiao, J. Xu, G. Cai, F. Ren, C. Jiang, E.P.L. Europhysics, Letters 93 (2011) 57009.
[5] M. Asgher, H.N. Bhatti, Ecol. Eng. 38 (2012) 79–85.
[6] I.M. Banat, P. Nigam, D. Singh, R. Marchant, Bioresour. Technol. 58 (1996) 217–227.
[7] E. Clarke, R. Anliker. Organic Dyes and Pigments, Anthropogenic Compounds, Springer, 1980, pp. 181–215.
[8] K. Kadirvelu, M. Kavipriya, C. Karthika, M. Radhika, N. Vennilamani, S. Pattabhi, Bioresour. Technol. 87 (2003) 129–132.
[9] T. Robinson, G. McMullan, R. Marchant, P. Nigam, Bioresour. Technol. 77 (2001) 247–255.
[10] S. Song, W. Gao, X. Wang, X. Li, D. Liu, Y. Xing, H. Zhang, Dalton Trans. 41 (2012) 10472–10476.
[11] T. Ghosh, J.-H. Lee, Z.-D. Meng, K. Ullah, C.-Y. Park, V. Nikam, W.-C. Oh, Mater. Res. Bull. 48 (2013) 1268–1274.
[12] S.N. Ahmed, W. Haider, Nanotechnology 29 (2018), 342001.
[13] M. Han, X. Chen, T. Sun, O.K. Tan, M.S. Tse, CrystEngComm 13 (2011) 6674–6679.
[14] T. Selvamani, B.G.S. Raj, S. Anandan, J.J. Wu, M. Ashokkumar, Phys. Chem. Chem. Phys. 18 (2016) 7768–7779.
[15] J. Tian, Y. Sang, G. Yu, H. Jiang, X. Mu, H. Liu, Adv. Mater. 25 (2013) 5075–5080.
[16] X. Zhang, Z. Ai, F. Jia, L. Zhang, J. Phys. Chem. C 112 (2008) 747–753.
[17] C. Xiao, H. Hu, X. Zhang, D.R. MacFarlane, ACS Sustain. Chem. Eng. 5 (2017) 10858–10863.
[18] C. Anderson, A.J. Bard, J. Phys. Chem. 99 (1995) 9882–9885.
[19] S. Chandrasekhar, P. Pramada, J. Majeed, J. Mater. Sci. 41 (2006) 7926–7933.

[20] S. Dagher, A. Soliman, A. Ziout, N. Tit, A. Hilal-Alnaqbi, S. Khashan, F. Alnaimat, J. A. Qudeiri, Mater. Res. Express 5 (2018), 065518.
[21] S. Ghorai, A. Sarkar, M. Raoufi, A.B. Panda, H. Schönherr, S. Pal, ACS Appl. Mater. Interfaces 6 (2014) 4766–4777.
[22] S. Liu, X. Chen, W. Ai, C. Wei, J. Clean. Prod. 212 (2019) 1062–1071.
[23] N. Saad, M. Al-Mawla, E. Moubarak, M. Al-Ghoul, H. El-Rassy, RSC Adv. 5 (2015) 6111–6122.
[24] N. Yuan, H. Cai, T. Liu, Q. Huang, X. Zhang, Adsorpt. Sci. Technol. 37 (2019) 333–348.
[25] C. Anderson, A.J. Bard, J. Phys. Chem. B 101 (1997) 2611–2616.
[26] L. Wang, X. Wang, J. Yin, Y. Zhu, C. Wang, Catal. Commun. 87 (2016) 98–101.
[27] I. Fatimah, N.I. Prakoso, I. Sahroni, M.M. Musawwa, Y.-L. Sim, F. Kooli, O. Muraza, Heliyon 5 (2019), e02766.
[28] Q.N. Khanh Nguyen, N.T. Yen, N.D. Hau, H.L. Tran, J. Chem. (2020) 2020.
[29] F. Dong, W.-K. Ho, S. Lee, Z. Wu, M. Fu, S. Zou, Y. Huang, J. Mater. Chem. 21 (2011) 12428–12436.
[30] K. Coenen, F. Gallucci, B. Mezari, E. Hensen, M. van Sint, Ann., J. CO_2 Util. 24 (2018) 228–239.
[31] B.H. Stuart, Infrared Spectroscopy: Fundamentals and Applications, John Wiley & Sons, 2004.
[32] M. Kruk, M. Jaroniec, Chem. Mater. 13 (2001) 3169–3183.
[33] J.A.A. Júnior, J.B. Baldo, New J. Glass Ceram. 4 (2014) 29.
[34] S. Liu, N. Zhang, Z.-R. Tang, Y.-J. Xu, ACS Appl. Mater. Interfaces 4 (2012) 6378–6385.
[35] R. Xu, M. Su, Y. Liu, Z. Chen, C. Ji, M. Yang, X. Chang, D. Chen, J. Clean. Prod. 242 (2020), 118366.
[36] L.O. de Brito Benetoli, B.M. Cadorin, V.Z. Baldissarelli, R. Geremias, I.G. de Souza, N.A. Debacher, J. Hazard. Mater. 237 (2012) 55–62.
[37] H. Gnaser, M.R. Savina, W.F. Calaway, C.E. Tripa, I.V. Veryovkin, M.J. Pellin, Int. J. Mass Spectrom. 245 (2005) 61–67.
[38] J. Rashid, S. Saleem, S.U. Awan, A. Iqbal, R. Kumar, M. Barakat, M. Arshad, M. Zaheer, M. Rafique, M. Awad, RSC Adv. 8 (2018) 11935–11945.
[39] M.A. Rauf, M.A. Meetani, A. Khaleel, A. Ahmed, Chem. Eng. J. 157 (2010) 373–378.
[40] S. Liu, A. Chen, Langmuir 21 (2005) 8409–8413.
[41] P. Paul, G.S. Kumar, J. Hazard. Mater. 184 (2010) 620–626.
[42] P. Paul, G.S. Kumar, Spectrochim. Acta Part A: Mol. Biomol. Spectrosc. 107 (2013) 303–310.
[43] X. Teng, J. Li, Z. Wang, Z. Wei, C. Chen, K. Du, C. Zhao, G. Yang, Y. Li, RSC Adv. 10 (2020) 24712–24720.
[44] O. Hamdaoui, E. Naffrechoux, J. Suptil, C. Fachinger, Chem. Eng. J. 106 (2005) 153–161.
[45] M.M. Maroto-Valer, I. Dranca, D. Clifford, T. Lupascu, R. Nastas, C.A.L. y Leon, Thermochim. Acta 444 (2006) 148–156.
[46] E. Sabio, E. González, J. González, C. González-García, A. Ramiro, J. Ganan, Carbon 42 (2004) 2285–2293.
[47] X. Yan, T. Ohno, K. Nishijima, R. Abe, B. Ohtani, Chem. Phys. Lett. 429 (2006) 606–610.